공학석사학위논문

개념설계단계에서의 소음 저감을 고려한 eVTOL UAM 기체 설계 방법론

Design Methodology of eVTOL Urban Air Mobility Vehicles Considering Noise Mitigation at Conceptual Design Stage

2023 년 2 월

서울대학교 대학원

항공우주공학과

김 호 진

개념설계단계에서의 소음 저감을 고려한 eVTOL UAM 기체 설계 방법론

Design Methodology of eVTOL Urban Air Mobility Vehicles Considering Noise Mitigation at Conceptual Design Stage

지도교수 이 관 중

이 논문을 공학석사 학위논문으로 제출함

2023 년 2 월

서울대학교 대학원

항공우주공학과

김 호 진

김호진의 공학석사 학위논문을 인준함

2023 년 2 월

위 원 장 김 규 홍 (인)

부위원장 이 관 중 (인)

위 원 권 기 범 (인)

Abstract

Design Methodology of eVTOL Urban Air Mobility Vehicles Considering Noise Mitigation at Conceptual Design Stage

Hojin Kim
Department of Aerospace Engineering
The Graduate School
Seoul National University

This article proposes a design methodology for UAM vehicles for noise mitigation at a conceptual design stage. A rotor analysis module for accurate noise prediction and a noise prediction module for a conceptual design stage are constructed. The rotor analysis module is developed for accurately predicting aerodynamic force distribution around rotor blades, thus enabling accurate noise prediction. This module consists of rotor analysis using BEMT or BET methods and CAMRAD II, and these methods exchange force distribution data, which is iterated in the module until aerodynamic force distribution by each method converges. The noise prediction module for a conceptual design stage uses compact loading assumption and dual compact loading assumption, therefore loading and thickness noise prediction are completed in a short time. The proposed design methodology is applied to a conceptual design of an eVTOL aircraft with the lift+cruise concept. Through the design optimization process, the necessity of considering noise impact at the conceptual design stage is demonstrated.

Key words: Advanced Air Mobility, Electric Vertical Takeoff and Landing Aircraft, Noise Prediction, Conceptual Design, Aerodynamic Coupling, Design Optimization
Student Number: 2021-21121

Table of Contents

Nomenclature

Symbols

$E_{\mathrm{on,off}}$	Turn-on and turn-off energies
f_{S}	Switching frequency
G	Change in the slope of the discharge curve due to current
$I_{\mathrm{d,q}}$	d- and q-axis current
I_{ref}	Reference current which is the on-state current after the commutation
I_s	Current space vector
I_{sm}	Voltage space vector
K	Primary dependency of voltage on the capacity discharged
$L_{\mathrm{d,q}}$	d- and q-axis inductance
M	Modulation index
MTOW	Maximum take-off gross weight
N	Number of the battery cell
P	Power
P_{Cu}	Copper loss
P_{Fe}	Iron loss
P_{lc}	Conduction loss
P_{ls}	Switching loss
$P_{\mathrm{no-load}}$	No-load power
P_{p}	Number of pole-pair
Q	Total capacity discharged up to the present instant
R	Internal resistance of the battery cell
R_{ce}	IGBT's differential resistance
R_{F}	Diode's differential resistance
R_{s}	Phase resistance
SP	Specific power
T	Torque
V_0	Open circuit (no load) voltage
V_{ce}	IGBT's threshold voltage
$V_{\mathrm{d,q}}$	d- and q-axis voltage

V_{DC}	DC link voltage
V_{F}	Diode's threshold voltage
V_{ref}	Reference voltage which is the blocking state voltage of the IGBT before the commutation
V_s	Voltage space vector
V_{sm}	Voltage constraint
β	Phase angle
η	Efficiency
λ_0	Stator permanent magnet flux linkage
ω_{b}	Base speed
ω_{e}	Electrical velocity

Chapter 1. Introduction

Since Uber announced its white paper [1] in 2016, interest in electric vertical takeoff and landing (VTOL) aircraft for urban air mobility (UAM) has been increasing. The advancements in electrification and automation technology accelerated the emergence of eVTOL aircraft. In addition to these technological developments that have made the emergence of eVTOL aircraft possible, noise emission caused by UAM vehicles is an important issue for the successful integration of UAM into the transport system[2]. This is because they are expected to fly frequent and short missions over populated areas at relatively low altitudes and they will operate with many numbers to conduct those missions [2, 3]. Due to the significance of the noise in introducing UAM into the new transport system, effective mitigation and prediction of the noise generated by eVTOL aircraft are considered essential [2, 4].

In addition to the increasing significance of the noise itself, the relative importance of the noise of eVTOL aircraft compared with conventional major requirements (e.g. range, seat capacity, and cruise speed) becomes large [5]. Also, major sizing parameters of aircraft are determined in the conceptual design stages, and these parameters including the gross weight of the aircraft can have the most impact on the acoustics of the aircraft[6]. Moreover, according to Faulkner[7], reducing the rotor tip speed is much more influential than changing other rotor design parameters in the detail design stage (eg. rotor tip and planform design) in reducing aeroacoustic noise from rotor blades. And compared with conventional helicopters with engines, eVTOL aircraft with electric propulsion systems (EPS) have a wider range of rotational speed. Therefore, compared with conventional helicopters, the noise impact of eVTOL aircraft can vary with a much larger range in the conceptual design stage where rotational speeds are determined. For all these reasons mentioned above, the noise impact of the eVTOL aircraft should be considered in the conceptual design stage, and by including the noise prediction in the early stage of design, decisions for the design of each eVTOL aircraft can be evaluated under control of the noise impact [8]. Furthermore, eVTOL aircraft can have design freedom in configuration (eg. multirotor type, lift+cruise type, and vectored thrust type) due to the advance in distributed electric propulsion (DEP) technology. Therefore, predicting the noise impact of each configuration in the conceptual design stage is necessary.

Meanwhile, rotors in DEP configuration show different aerodynamic characteristics from an isolated rotor. Zhou et al. [9] investigated variations in the aerodynamic and aeroacoustic performances caused by the rotor-to-rotor interactions in small UAVs through experiments. The magnitude of thrust fluctuation and noise increased in a dramatic way as the distance between each rotor became smaller, which was caused by complex flow interactions. Shukl et al. [10, 11] found the same trends in performance variation with respect to the separation distance, and tip vortices and trailing edge vortex sheets were visualized using high-speed stereo particle image velocimetry (SPIV) system. With a small separation distance, tip vortices from each rotor were split into small spots of high vorticity within a rotation and did not follow normal helical trajectories. Healy et al. [12] conducted an investigation into interactional aerodynamics caused by the laterally and longitudinally canted rotors using the commercial Navier-Stokes CFD solver, AcuSolve[13]. Five two-rotor cases where front rotors and aft rotors with different cant angles were positioned in line with the flow direction were solved, and penalties in thrust and change in pitching and rolling moments for aft rotors in each case were quantitatively compared with a single rotor case. Since the front rotor caused downwash on the aft rotor, aft rotors always showed reduced thrust and nose-down pitching moment due to decreases in the lift at the front part of the aft rotor disk. The case with the longitudinal inner cant showed 21% of thrust penalty and 95% of pitching moment change in the aft rotor. And simple rotor analysis models (eg. blade element theory or blade momentum theory) that were normally used in the conceptual design frameworks cannot capture the interactional aerodynamics and aeroacoustics of adjacent rotors. Therefore, using these analysis models can cause large gaps with real aerodynamic and aeroacoustic performances and finally undesired repetitions of feedback in the design process.

On the other hand, some other computational methods for rotor aerodynamics have the capability of capturing rotor-rotor interactions [12, 14–24]. Especially, rotor free wake modeling[25–33] has proved its capability of predicting aerodynamic interactions between rotors, which are caused by tip vortices from each rotor. In the study by Guan et al[22], the acoustic experiment of a dual-rotor system by NASA

[34] was chosen for verification of the multirotor aerodynamic noise prediction framework using free wake modeling. The measured noise directivity was selected as validation data and the in-plane noise was well captured by free wake modeling. In the case of the ouf-of-plane results, the simulation showed good consistency with the test, and the mean square error in terms of amplitude was about 2dB [34]. Therefore, when conducting sizing and noise prediction in the conceptual design stage of eVTOL aircraft with DEP configuration, using rotor aerodynamic analysis models like free wake modeling can provide more realistic results[35] than simple rotor analysis models like BET or BEMT, which are not capable of capturing the rotor interaction effects.

In this study, the multidisciplinary conceptual design of eVTOL aircraft was conducted, and, in addition to the sizing parameters of eVTOL aircraft, the noise impact was calculated. In the design process, for capturing the aerodynamic and aeroacoustic interactions under the DEP configuration with the close proximity between rotors, aerodynamic coupling between a lifting line-based analysis with the free wake modeling and a conceptual design framework of eVTOL aircraft was performed. For the lifting line-based analysis model and the conceptual design framework of eVTOL aircraft, the comprehensive analysis model of rotorcraft aerodynamics and dynamics II (CAMRAD II) [36] and rotorcraft initial sizing and performance estimation tool-kit+ (RISPECT+) [37] were used respectively. In this aerodynamic coupling, rotor aerodynamic analysis results from BET and BEMT modules in RISPECT+ are corrected by the results from CAMRAD II, which can capture unsteady loading and fluctuation in aeroacoustic pressure change caused by the interactions between each rotor and tip vortices from other rotors. By using this coupling between CAMRAD II and the rotor analysis model in RISPECT+, aerodynamic and aeroacoustic performance changes under rotor-rotor interaction were captured. A parametric study of design variables in eVTOL aircraft was performed for an enhanced understanding of critical design variables affecting the sizing parameters and noise impact of eVTOL aircraft with the DEP configuration. Plus, a design optimization was conducted using RISPECT+ with the coupling method, from which a guideline for conducting an initial sizing of eVTOL aircraft with a low noise impact is suggested.

The remainder of this paper is organized as follows. Chapter 2 briefly introduces the overall flow of RISPECT+. Chapters 3 and 4 detail the four sizing modules in RISPECT+ and the noise analysis module respectively. Chapter 5 presents the parametric study results of an eVTOL aircraft using the proposed framework. Chapter 6 provides the optimization results of the eVTOL aircraft. Finally, Chapter 7 discusses the results and provides the conclusion of the paper.

Chapter 2. Conceptual Design Framework for eVTOL Aircraft : RISPECT+

In this study, the conceptual design framework RISPECT+ [38] (Rotorcraft Initial Sizing and Performance Estimation Code and Toolkit+) is used. RISPECT+ was developed as a program to provide performance analysis and initial sizing results for VTOL aircraft with various kinds of configurations. It also provides EPS analysis modules, therefore accurate weight estimation of EPS for eVTOL aircraft is possible [39]. As in Figure 2-1, RISPECT+ consists of three steps. In step one, the initial sizing of an eVTOL aircraft using input design conditions is conducted. Modules in this step consist of 1) a flight analysis module, 2) a propulsion system sizing module, 3) a mission analysis module, and 4) a weight estimation module. In step two, aerodynamic model correction and noise analysis are conducted. In this step, by coupling the flight analysis module in RISPECT+ and CAMRAD II, accurate aerodynamic force calculation is conducted. In addition, by using the newly developed noise prediction module, the noise impact of each eVTOL aircraft is evaluated. In step 3, by calculating each design's fitness, design optimization is conducted. The overall flow of RISPECT+ with noise prediction is in Fig. 2-1.

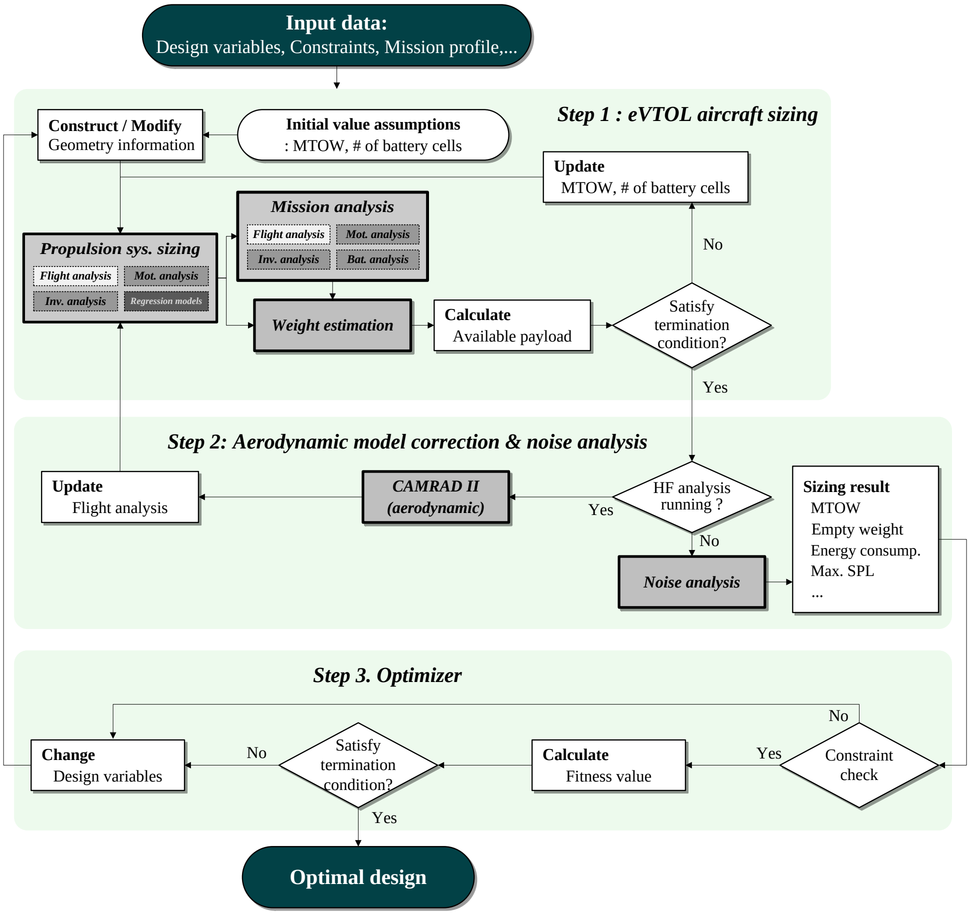

Figure 2-1. Flowchart of the conceptual design methodology using RISPECT+.

Chapter 3. Sizing Module in RISPECT+

Sizing modules in RISPECT+ consist of a flight analysis module, propulsion system sizing module, mission analysis module, and weight estimation module. Each module is explained in this section.

3.1. Flight analysis module

As mentioned above, the previous version of RISPECT+ uses BEMT and BET methods for fast estimation of rotor performance at a conceptual design stage[38]. These methods can be considered as suitable if calculating rotor performance and conducting initial weight estimation of eVTOL aircraft are the only interests at the conceptual design stage. However, with respect to accurately predicting noise impacts caused by multiple rotors, these methods are not proper because they assume that there is no aerodynamic interaction between each rotor, therefore neglecting aerodynamic force distribution change around rotor blades due to the rotor-rotor interaction effect. Specifically, BEMT method calculates the inflow ratio, $\boldsymbol{\lambda_i}$ across the radial direction of the rotor blade and determines lift coefficient, $\boldsymbol{C_l}$ and drag coefficient, $\boldsymbol{C_d}$ at each blade section, assuming that there is no rotor-rotor interaction. Therefore, all rotors have the same rotational speed and $\boldsymbol{C_l}$ and $\boldsymbol{C_d}$ distribution. However, when more than two rotors are under rotor-rotor interaction, the aerodynamic force distribution is influenced by the interaction, the aerodynamic force distribution is influenced by the interactions. Therefore, noise source generation is affected by the interactions [40].

For this reason, in this study, RISPECT+ & CAMRAD II coupling is used for accurately predicting aerodynamic force distribution around rotor blades under rotor-rotor interaction. The flow chart of RISPECT+ & CAMRAD II coupling is in Fig. 3-1.

First, for a given set of input design variables, RISPECT+ conducts initial sizing for an eVTOL aircraft as seen in Fig. 3-1. In this process, RISPECT+ only uses

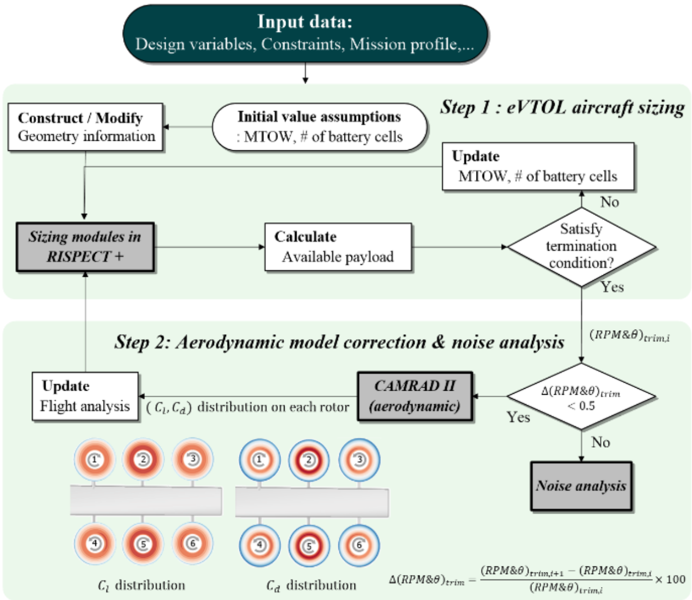

Figure 3-1. RISPECT+ & CAMRAD II Coupling

BEMT / BET methods for predicting aerodynamic force distribution around rotor and propeller blades and calculates control input sets of rotors and propellers for a trimmed condition at each mission segment. Then, the control input sets at each mission segment are provided to CAMRAD II as input operating conditions ,and aerodynamic force distribution around rotor and propeller blades are caculated using the free wake model. Now the force distribution at each rotor and propeller blade obtained by CAMRAD II is provided to RISPECT+, and RISPECT+ conducts flight analysis modified by the force distribution and resizes the eVTOL aircraft. In this sizing process, RISPECT+ again calculates control input sets of rotors and propellers for a trimmed condition, and they are used again by CAMRAD II as input operating conditions. This procedure repeats until the difference of control inputs for a trimmed condition between present and previous step is less than 1%. After the procedure ends, final gross weight of the eVTOL aircraft is determined and noise analysis module calculates noise impacts of the eVTOL aircraft. Figure 3-2 shows the process where C_l and C_d distributions calculated by RISPECT+ and CAMRAD II converge to each other.

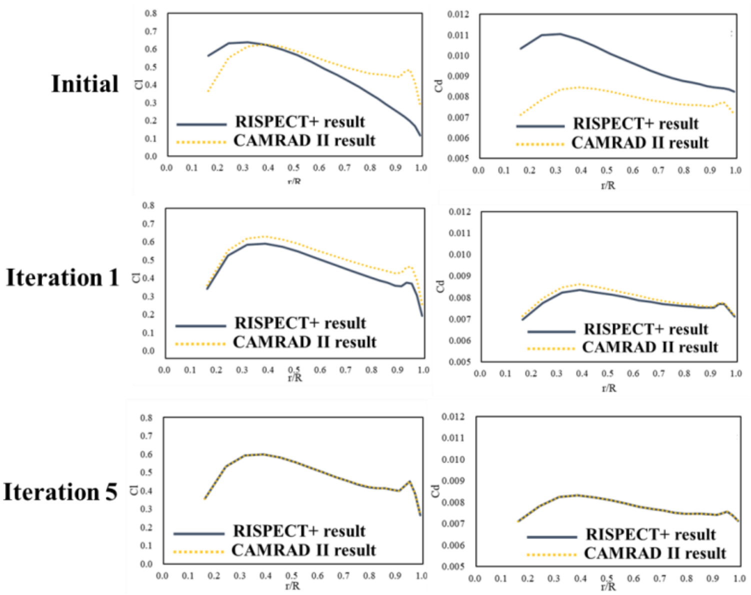

Figure 3-2. Convergence history of RISPECT+ & CAMRAD II Coupling

3.2. Electric propulsion system sizing module

3.2.1. Motor analysis

For the analysis of the permanent magnet synchronous motor (PMSM), three control strategies that can help an efficient operation of the PMSM are utilized in this study, and they are described below [41].

Maximum torque per ampere (MTPA) control: This concept is a control method to obtain the maximum torque under the given stator current amplitude by controlling d- and q- axis current components.

Field weakening or Maximum torque per voltage control: These concepts increase the rotational speed by reducing electromagnetic torque. Because propulsive loads (fan, rotor, or propeller) reach high power and high speed simultaneously, field weakening and maximum torque per voltage control strategies to achieve high speed at the expense of torque are not useful for aircraft propulsion.

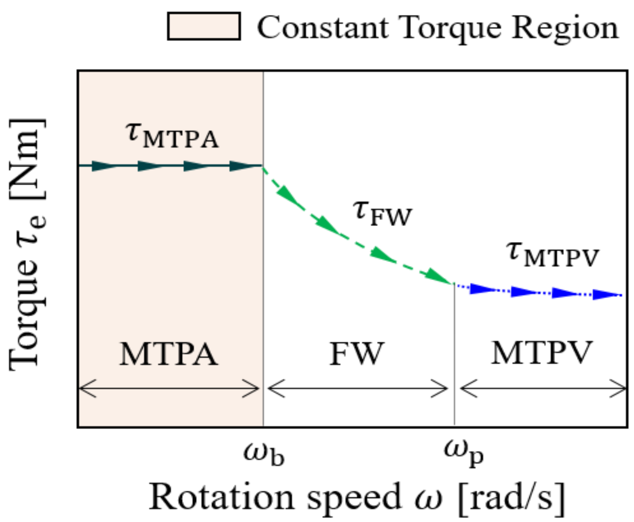

Figure 3-3. Example of the PMSM control using three control strategies

Figure 3-3 shows an example of the PMSM control using three control strategies mentioned above and Figure 3-4 shows the input current vector trajectory at control strategy for efficient operation of the PMSM.

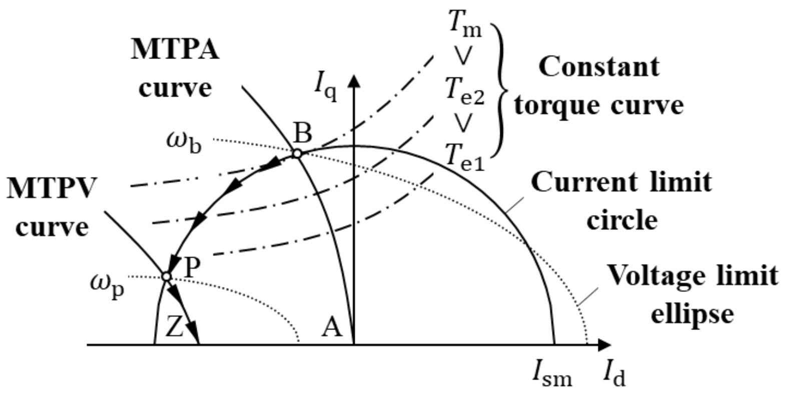

Figure 3-4. Input current vector trajectory

As it can be seen in Figure 3-3, which type of control strategy will be used basically depends on the torque and corresponding rotational speed of motor. Therefore, baseline speed $\boldsymbol{\omega_b}$ and critical speed $\boldsymbol{\omega_p}$ should be obtained first to determine a control startegy at a given torque and rotational speed.

Electromagnetic torque $\boldsymbol{T_e}$ can be obtained by using Eq. (3-1)

$$(3\text{-}1)\quad \boldsymbol{T_e = \frac{3}{2}\frac{P}{2}\left[\lambda_0 I_q + \left(L_d - L_q\right) I_d I_q\right]}$$

$$\boldsymbol{= \frac{3}{2}\frac{P}{2}\left[\lambda_0 I_s sin\beta + \frac{\left(L_d - L_q\right)}{2} I_s sin2\beta\right]}$$

And by differentiating equation (3-1) with respect to the phase angle $\boldsymbol{\beta}$, the optimal d- and q- axis current components that maximize $\boldsymbol{T_e}$ can be calcuated. The optimized curruent component of each axis are in Eqs. (3-2) and (3-3).

(3-2) $\boldsymbol{I_{dm}} = \frac{\lambda_0}{2(L_q - L_d)} - \sqrt{\frac{\lambda_0}{16(L_q - L_d)^2} + \frac{I_{sm}^2}{2}}$

(3-3) $\boldsymbol{I_{qm}} = \sqrt{I_{sm}^2 - I_{dm}^2}$

In addition, the baseline speed $\boldsymbol{\omega_b}$ until which the PMSM can maintain maximum torque under current limit and voltage limit can be obtained by using Eq. (3-4). And as it can be seen in Figure 3-3, the limiting point for MTPA control is where MTPA curve, current limit curve and voltage limit curve cross.

(3-4) $\boldsymbol{\omega_b} = \frac{V_{sm}}{\sqrt{(L_d I_{dm} + \lambda_0)^2 + (L_q I_{qm})^2}}$

If motor speed of the PMSM becomes larger than $\boldsymbol{\omega_b}$, the PMSM applies FW control under the given voltage limit condition. Since maximum terminal volatge becomes smaller as motor speed becomes larger, allowable torque decreases with the increase of motor speed. Current component of d- and q- axis under FW control can be determined by using Eqs. (3-5) and (3-6)

(3-5) $\boldsymbol{I_{\mathrm{dn}}} = -\frac{-2L_{\mathrm{d}}\lambda_0 + \sqrt{(2L_{\mathrm{d}}\lambda_0)^2 - 4(L_{\mathrm{d}}^2 - L_{\mathrm{q}}^2)\left(\lambda_0^2 + L_{\mathrm{q}}^2 I_{\mathrm{m}}^2 - \left(\frac{V_{\mathrm{m}}}{\omega_{\mathrm{e}}}\right)\right)}}{2(L_{\mathrm{d}}^2 - L_{\mathrm{q}}^2)}$

(3-6) $\boldsymbol{I_{\mathrm{qn}}} = \sqrt{I_{\mathrm{sm}}^2 - I_{\mathrm{dn}}^2}$

When the motor speed increases until critical speed $\boldsymbol{\omega_p}$, FW control is the best strategy for providing the largest torque. However, if the motor speed becomes larger than $\boldsymbol{\omega_p}$, the PMSM can provide higher torque by using MTPV control than FW control. The critical speed $\boldsymbol{\omega_p}$ can be obtained by equating the torque produced by FW $\boldsymbol{T_n}$ and the torque produced by MTPV control $\boldsymbol{T_p}$ and finding the $\boldsymbol{\omega_p}$ that satisfies that equation. $\boldsymbol{T_n}$ can be calcualted by Eqs. (3-1), (3-5) and (3-6); $\boldsymbol{T_p}$ can be calculated by Eqs. (3-1), (3-7), (3-8) and (3-9).

(3-7) $\boldsymbol{I_{\mathrm{dp}}} = -\frac{\lambda_0}{L_{\mathrm{d}}} - \Delta \boldsymbol{I_{\mathrm{d}}}$

(3-8) $\boldsymbol{I_{\mathrm{qp}}} = \frac{\sqrt{(V_{\mathrm{sm}}/\omega_{\mathrm{e}})^2 - (\Delta I_{\mathrm{d}} L_{\mathrm{d}})^2}}{L_{\mathrm{q}}}$

(3-9) $\Delta \boldsymbol{I_{\mathrm{d}}} = \frac{\frac{L_{\mathrm{q}}}{L_{\mathrm{d}}}\lambda_0 + \sqrt{\left(\frac{L_{\mathrm{q}}}{L_{\mathrm{d}}}\lambda_0\right)^2 + 8\left(\frac{L_{\mathrm{q}}}{L_{\mathrm{d}}} - 1\right)^2 \left(\frac{V_{\mathrm{sm}}}{\omega_{\mathrm{e}}}\right)}}{4(L_{\mathrm{d}} - L_{\mathrm{q}})}$

After obtaining $\boldsymbol{\omega_b}$ and $\boldsymbol{\omega_p}$, motor efficiency can be calculated as Eq. (3-4) using the current and voltage component at each operating control strategy and motor parameters determined through motor sizing procedure.

(3-10) $\boldsymbol{\eta_{\mathrm{motor}}} = \frac{P_{\mathrm{mech}}}{P_{\mathrm{mech}} + P_{\mathrm{iron}} + P_{\mathrm{copper}} + P_{\mathrm{no-load}}}$

More detailed information about each loss component can be found in [42].

3.2.2. Inverter analylsis module

In this study, inverters with six pairs of insulated gate bipolar transistor (IGBT) and diode are used for calculating inverter efficiency.

For the inverter composed of pairs of IGBT and diode, power loss by the inverter, $\boldsymbol{P_{loss,inv}}$ can be obtained by the sum of switching loss, $\boldsymbol{P_{ls}}$ and conduction loss, $\boldsymbol{P_{lc}}$ and they are calculated as in [43, 44].

(3-11) $\boldsymbol{P_{loss,inv}} = \boldsymbol{6} \times (\boldsymbol{P_{ls}} + \boldsymbol{P_{lc,I}} + \boldsymbol{P_{lc,D}})$

Since input voltage and current of motor and output voltage of battery are needed for calculating power loss by the inverter. Therefore, motor, inverter and battery analysis should be conducted at every time step among every mission segment.

3.2.3. Battery analysis module

In this study, nearly-linear discharge model is used for battery analysis. Since the model considers output voltage drop effect of battery as discharge undergoes, it can accurately calculate battery cell curruent and voltage and therefore the inverter efficiency and battery depth of discharge (DOD). Mathmatical modeling of battery cell voltage is in Eq. (3-12) [45] .

(3-12) $$\boldsymbol{V = 0.5\left[(V_0 - KQ) + \sqrt{(V_0 - KQ)^2 - 4(RP + GQP)}\right]}$$

3.3. Mission analysis module

At mission analysis module, flight analysis explained in Chap. 3.1. is conducted at all mission segements such as take off, hovering and cruising and rotor operation indices such as required power and rotational speed are calculated. Then, by using EPS analysis moudles mentioned in Chap. 3.2., the total discharged battery capacity is calculated and finally the minimum numer of battery cells to satisfy the whole mission profile is determined.

3.4. Weight estimation module

Weight estimation module calculates the weight of each component of eVTOL aircraft such as motor, inverter, wing and fuselage using table data. More detailed information can be found in [42].

Chapter 4. Noise Prediction in RISPECT+

In this study, only loding noise and thickness noise are calculated for predicting noise from eVTOL aircraft. Mathmatical modeling of each noise component is described below.

4.1. Loading noise

In this study, Farasst's 1A loading noise formula [46] with compact loading assumption [47] is used for calculating loading noise from rotors. In compact loading assumption, sectional loading is assumed to be applied at c/4 of airfoil and that point is used as a noise source for loading noise calculation. By using this assumption, surface integral in original Farassat's 1A loading noise formula changes to line integral as in Eq. (4-1), therfore flowfield data from comprehensive analysis code can be used for loading noise prediciton and time efficient noise prediction is possible.

$$(4\text{-}1)\quad \boldsymbol{4\pi p_L'(x,t) = \frac{1}{c}\int_{f=0}\left[\frac{\dot{L_r}}{r|1-M_r|^2}\right]_{ret} dR + \int_{f=0}\left[\frac{L_r-L_M}{r|1-M_r|^2}\right]_{ret} dR}$$

$$\boldsymbol{+\frac{1}{c}\int_{f=0}\left[\frac{L_r\left(r\dot{M}_r + \mathrm{c}\mathrm{M}_r - \mathrm{c}\mathrm{M}^2\right)}{r^2|1-M_r|^3}\right]_{ret} dR}$$

4.2. Thickness noise

For calculating thickness noise prediction, Farassat's 1A thickness noise formula with dual compact loading assumption is used in this study [48]. In dual compact loading assumption, all chordwise nosie sources along blade surface are replaced by two loading sources of which loading values are $\boldsymbol{\rho_0 c_0^2 h}$ respectively and directions are opposite to that of each other as in Figure 4-1. As in compact loading assumption, this assumption can help time efficient calculation of thickness noise. Validations between thickness noise calculated by normal thickness noise formula and dual compact loading assumption are shown in Figure 4-2.

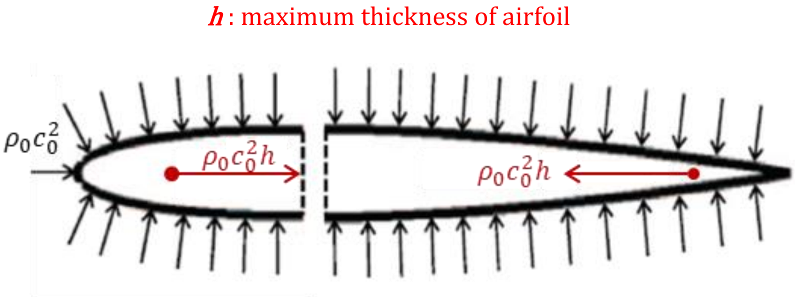

Figure 4-1. Dual compact laoding assumption for thickness noise prediction

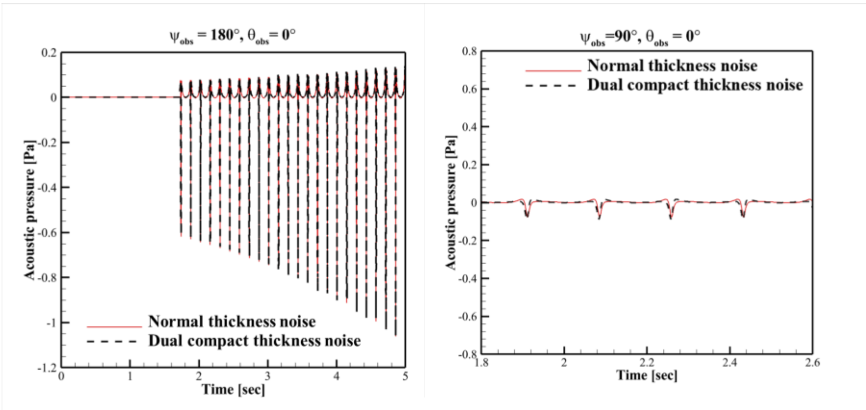

Figure 4-2. Comparison between normal thickness noise formula and dual compact loading assumption

4.3. Retarded-time algorithm

In this study, as a retarded-time algorithm, soure-time-dominant algorithm was used [49]. In this algorithm source time is regarded as the primary time (dominant time). For calculating aeroacoustic pressure change at observers, the source time is chosen first and then determine the time when the signal will reach the observer. Next, acoustic pressures are interpolated based on desired observer times.

Chapter 5. Parametric Study of an eVTOL Aircraft Design Using the Framework

Using the proposed framework, parametric study was conducted to see an effect of each design variable on the quantities of interest (QOIs). In this study, QOIs consist of major QOIs such as gross weight and noise impact of an eVTOL aircraft and minor QoIs such as motor weight and hovering tip Mach number.

5.1. Problem definition

Table 5-1. Geometric data of Wisk Cora[50]

Rotor[1]	Disk loading (per rotor): 14.76 lb/ft2 Aspect ratio: 3.17 Taper ratio: 0.75 Collective pitch: 13.5 deg
Wing[1]	Wing loading: 19.45 lb/ft2 Aspect ratio: 12.4 Taper ratio: 1
Propeller[1]	Radius: 3.5 ft Solidity: 0.1

Wisk Cora was used as the baseline eVTOL aircraft and its geometric data is in Table 5-1., and its three-dimensional modeling is in Figure 5-1. For mission profile of the eVTOL aircraft, simplified version of Uber Elevate mission profile [50] was used as in Figure 5-2.

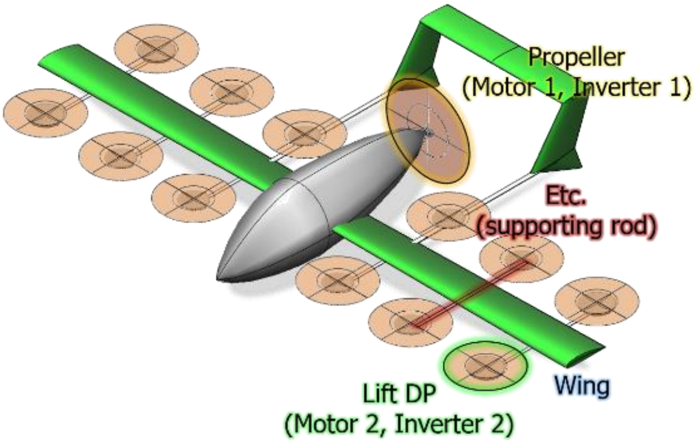

Figure 5-1. Three-dimensional modeling of Wisk Cora[38]

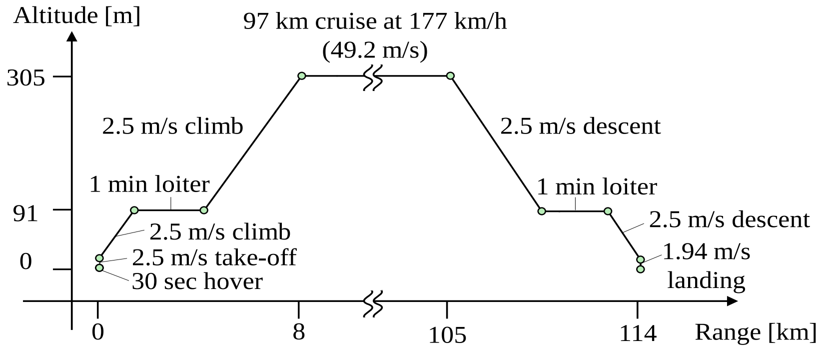

Figure 5-2. Uber Elevate mission profile[50]

For the parametric study, 12 design variables are used, and the target payload of eVTOL aircraft is set as 400 lb. Details about each design variable and payload are listed in Table 5-2.

Table 5-2. Design variables & payload

DV	**Rotor**			
	Radius [ft]	Chord [ft]	Twist [deg]	Incidence angle [deg]
	$\mathbf{1.8 < R_{rotor} < 2.4}$	$\mathbf{0.5 < c_{rotor} < 0.8}$	$\mathbf{-15 < \theta_{tw,rotor} < 0}$	$\mathbf{13.5 < \theta_{0,rotor} < 23.8}$
	Propeller			
	Radius [ft]	Chord [ft]	Twist [deg]	Rotational speed [RPM]
	$\mathbf{3 < R_{prop} < 4.2}$	$\mathbf{0.3 < c_{prop} < 0.43}$	$\mathbf{-18 < \theta_{tw,prop} < -12}$	$\mathbf{1950 < RPM_{prop} < 2640}$
	Wing			
	Span [ft]	Aspect ratio	Incidecne angle [deg]	Supporting rod length [ft]
	$\mathbf{32.8 < Span_{wing} < 43.2}$	$\mathbf{10 < AR_{wing} < 15}$	$\mathbf{10 < \theta_{wing} < 15}$	$\mathbf{6.4 < l_{rod} < 9.6}$
Payload	400 lb (fixed)			

For assessing the noise impact of each eVTOL aircraft design, the quantitative criteria suggested in Uber Elevate was used. According to Uber Elevate white paper, UAM departing from or landing at vertiports should satisfy noise level criteria that maximum A-weighted overall sound pressure level (OASPL) on the ground, $\boldsymbol{L_{Amax}}$ is approximately 62 dBA at 500ft [1]. Therefore, $\boldsymbol{L_{Amax}}$ on the ground while an eVTOL aircraft is hovering at 500 ft was chosed as an assesment for noise impact of each eVTOL aircraft design. For calculating $\boldsymbol{L_{Amax}}$, $\boldsymbol{C_l}$ & $\boldsymbol{C_d}$ distribution and rotational speed of each rotor determined through the sizing procedure mentioned in Chapter 3 are provided to the noise prediction module. Then, using the noise prediction module, acoustic pressure change is calculated at each point on the ground which is 500 ft below an eVTOL aircraft, and A-weighted OASPL is calculated at each point. Finally, L_{Amax} is determined among all points on the ground. For example, noise countour of the baseline eVTOL aircraft is in Figure 5-3 and calculated L_{Amax} is 74.8 dBA

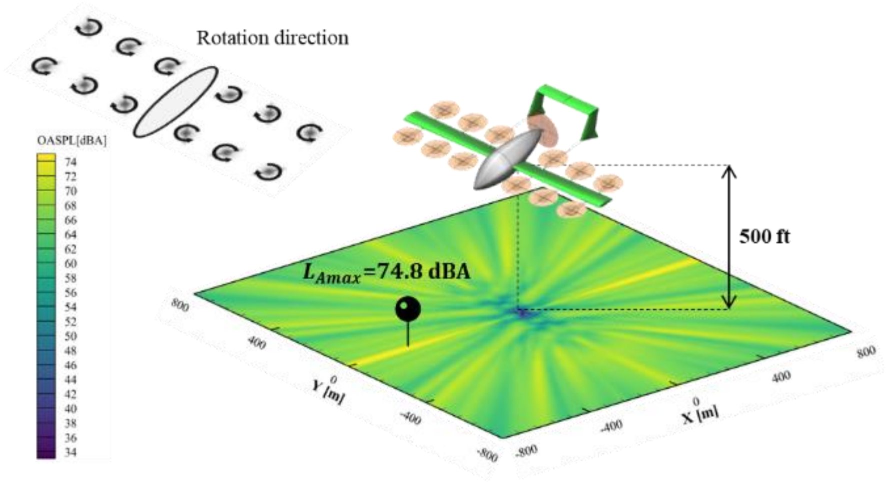

Figure 5-3. Noise contour (A-weighted OASPL) of the baseline eVTOL aircraft on the ground

5.2. ANOVA and sensitivity analysis

For conducting analysis of varinace (ANOVA) and sensitivity analysis between design variables and QOIs, a surrogate model was construced using Gaussian Process Regression (GPR) where total 3000 points were sampled through latin hypercube sampling (LHS) [51]. GPR assumes likelihood function as Gaussian and applies posterior Gaussian process for predicting functions [52]. Validation of each GPR model is in Appendix. However, in this sizing problem, not all sets of design variables can satify the target payload even though the sizing moudle in RISPECT+

increases the gross weight to get the payload of 400 lb. For example, if $\boldsymbol{R_{prop}}$ of an eVTOL aircraft gets smaller, a higher propeller collective pitch at the cruising mission is required. And if $\boldsymbol{R_{prop}}$ is too small, the required collective pitch at the cruising mission is too high, and the input collective pitch crosses the limit where stall occurs, showing an unacceptable performance. Finally, the eVTOL aircraft with too small $\boldsymbol{R_{prop}}$ cannot complete the cruising mission, therefore is not capable of satisfying the target payload. For this reason, another surrogate model should be constructed for classifying the whole design space into feasible and infeasible space. For this, we used Gaussian Process Classifier (GPC). GPC uses Laplace approximation for the posterior process because targets are discrete class labels, and is suitable for binary classification or multi-class classification [52]. In this problem, target labels are 'feasible' and 'infeasible', therefore GPC for a binary problem is used. Validation of GPC is in Appendix.

For analyzing relations between design variables and QOIs, Analysis of variance (ANOVA) was performed. ANOVA is a method that quantitatively estimates global sensitivity of each design variable by calculating the ratio of a covariance of a design variable to a total variance of all design variable sets [53]. In this study, ANOVA was performed for two major QOIs, $\boldsymbol{GW}$ and $\boldsymbol{L_{Amax}}$. Furthermore, sensitivity analysis was performed for analyzing relations between design variables and QOIs in more detail. In this analysis, the baseline eVTOL aircraft was chosen as a reference point, and crossings between two red dotted lines mean the reference point. Areas with gray color mean infeasible design spaces that cannot satisfy the target payload, which are classified by the GPC model mentioned above.

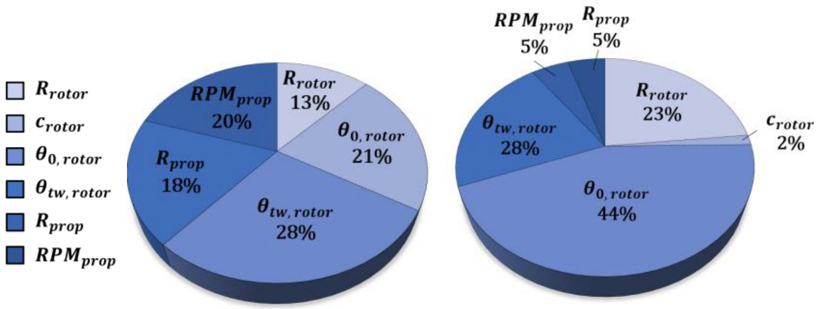

(a) GW (b) L_{Amax}

Figure 5-4. ANOVA results

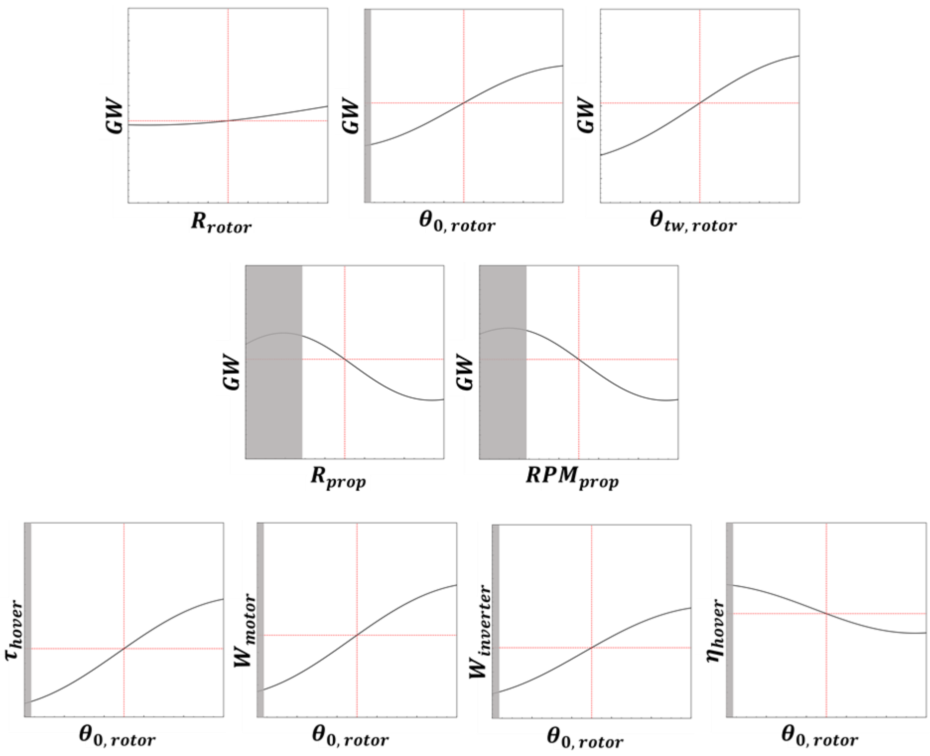

Figure 5-5. Sensitivity analysis results for GW (1)

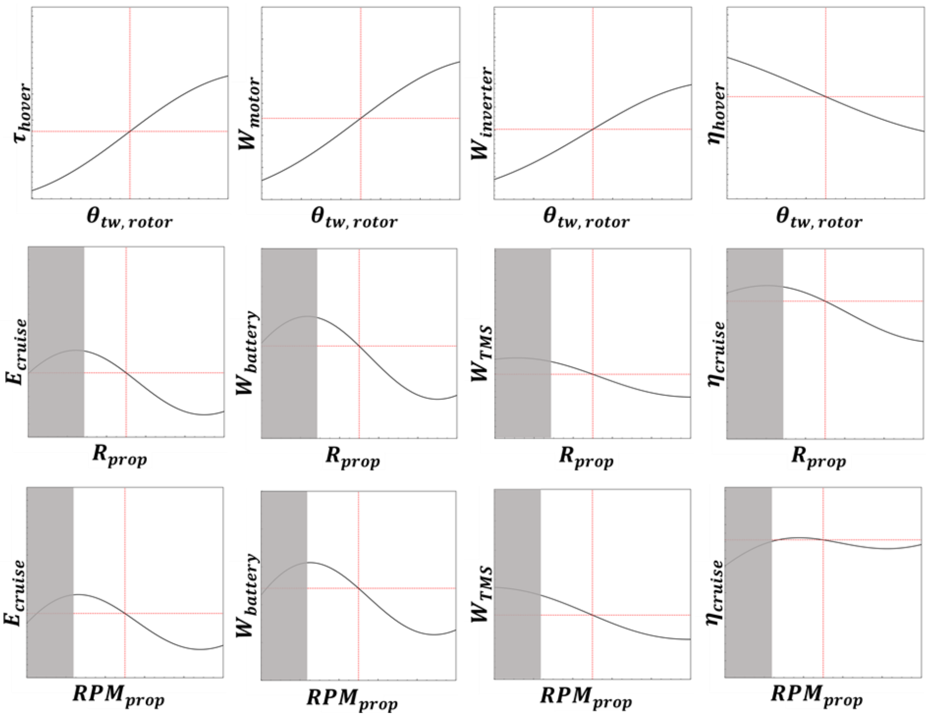

Figure 5-6. Sensitivity analysis results for GW (2)

As in Figure 5-4., through ANOVA for $\boldsymbol{GW}$, $\boldsymbol{\theta_{0,rotor}}$, $\boldsymbol{\theta_{tw,rotor}}$ and $\boldsymbol{R_{rotor}}$ are identified as having significant effects on $\boldsymbol{GW}$. The reason for their influences is that hovering performance of a rotor is closely related with the motor size. Maximum required power and torque occur at the hovering mission, and as mentioned in Chap. 3.2.1, motor sizing is conducted based on the maximum required torque among all mission segments. Therby, the hovering performance is important in deciding the weight of motor. And the weight of other subsystems such as inverters and wiring increases in proportion to the increase of the motor weight. Therefore, $\boldsymbol{\theta_{0,rotor}}$ and $\boldsymbol{\theta_{tw,rotor}}$ that are closely related with hovering performance are influential in determining the gross weight. These relations are confirmed in the sensitivity analysis in Figure 5-5. As $\boldsymbol{\theta_{0,rotor}}$ increases, the required torque, $\boldsymbol{\tau_{hover}}$, for the hovering mission increases, which leads to the increase of the motor weight, $\boldsymbol{W_{motor}}$. This is accompanied by the weight increase of the inverter, $\boldsymbol{W_{inverter}}$, thus causing the total weight increase. Furthermore, it is shown that the increase of $\boldsymbol{\theta_{0,rotor}}$ corresponds with the decrease of the total system efficiency at the hovering mission, $\boldsymbol{\eta_{hover}}$. This is same for $\boldsymbol{\theta_{tw,rotor}}$ as in Figure 5-5. In addition, as in Figure 5-4, $\boldsymbol{R_{prop}}$ and $\boldsymbol{RPM_{prop}}$ are also recognized as important design variables when deciding the gross weight. This is because the weight of battery is closely related with the cruising performance. As mentioned in Chap. 3.3, the number of parallel and serial battery cells is determined by calculating required energy through whole mission profile. And since the duration of the cruising mission is about 50 minutes, used energy at the cruising mission takes most of the total used energy. For this reason, battery weight is closely related with the cruising performance. And similar with a motor, the weight of other electric propulsion subsystems such as thermal management sysemt (TMS) increases as the weight of the battery increases, design varaibles such as $\boldsymbol{R_{prop}}$ and $\boldsymbol{RPM_{prop}}$ have large impacts on the gross weight. We can validate these correlations in depth by conducting sensitivity analysis. As in Figure 5-6, as $\boldsymbol{R_{prop}}$ increases, the required energy, $\boldsymbol{E_{cruise}}$, for the cruising mission decreases, thus leading to the increase of the battery weight, $\boldsymbol{W_{battery}}$ and the TMS weight, $\boldsymbol{W_{TMS}}$. But this trend changes to the opossite after a point because as $\boldsymbol{R_{prop}}$ increases, he tip speed of a propeller increases, which is followed by the increase of the required power for the propeller. This is same for $\boldsymbol{RPM_{prop}}$ as in Figure 5-6.

When ANOVA is conducted for $\boldsymbol{L_{Amax}}$, $\boldsymbol{\theta_{0,rotor}}$, $\boldsymbol{\theta_{tw,rotor}}$ and $\boldsymbol{R_{rotor}}$ are the most influential in deciding the noise impact. This is because the magnitude of aeroacoustic noise from rotors largely depends on the rotor tip speed, which corresponds with Faulkner's research on the relation between noise and the tip speed [7]. On top of that, this relation can be verified in this study via sensitivity analysis between these three design variables and the hovering tip Mach number of rotors, $\boldsymbol{M_{tip,hover}}$. As in Figure 5-6., when $\boldsymbol{\theta_{0,rotor}}$ increases, $\boldsymbol{M_{tip,hover}}$ decreases and even though $\boldsymbol{GW}$ increases as $\boldsymbol{\theta_{0,rotor}}$ increases, thus enlarging sectional loading on the rotor blade, the increase of $\boldsymbol{M_{tip,hover}}$ overwhelms enlarged sectional loading, therefore $\boldsymbol{L_{Amax}}$ decreases. Likewise, as the absolute magnitude of $\boldsymbol{\theta_{tw,rotor}}$ decreases (less twisted), the average sectional twist angle increases, thus reducing $\boldsymbol{M_{tip,hover}}$. And It finally causes the drop in $\boldsymbol{L_{Amax}}$ in spite of the increase of sectional loading caused by surging $\boldsymbol{GW}$. Lastly, as $\boldsymbol{R_{rotor}}$ increases, $\boldsymbol{M_{tip,hover}}$ decreases. And enlarged sectional loading caused by the increase of $\boldsymbol{GW}$ and expansion of thickness noise sources due to the increase of $\boldsymbol{R_{rotor}}$ are overwhelmed by the reduction in $\boldsymbol{M_{tip,hover}}$, thus causing drop in $\boldsymbol{L_{Amax}}$.

Since in this study, only maximum value of A-weighted OASPL is considerd as noise impact of eVTOL aircraft, noise contours for three designs (Design A, B and C) are depicted in Figure 5-8. In addition, sectional loading distribution around rotor blades for each design is portrayed in Figure 5-8. And Table 5-3 explains QoIs of each design.

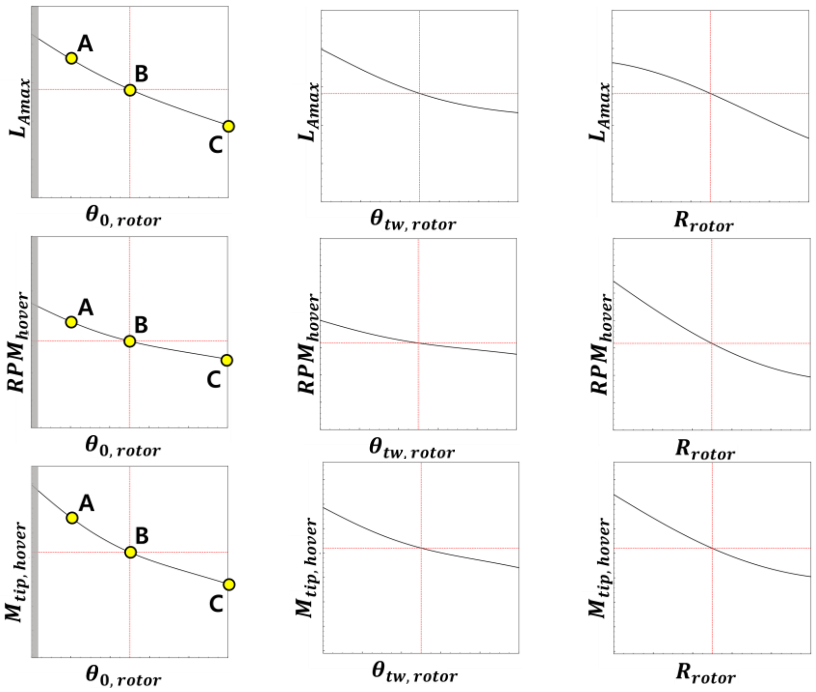

Figure 5-7. Sensitivity analysis for L_{Amax}

Table 5-3. QoIs of each design

QoIs	Design A	Design B (baseline)	Design C
GW [lb]	2734	2966	3588
L_{Amax}[dBA]	85.89	78.42	70.09
$M_{tip,hover}$	0.64	0.6	0.55

As it can be seen in Figure 5-8, when a design changes from *Design A* to *Design C*, not only L_{Amax} drops from 85.89 dBA to 70.09 dBA, but also overall OASPL on the ground decreases. Furthermore, as mentioned above, even though lift around rotor blades is larger in *Design C* than in *Design A* due to larger $\boldsymbol{GW}$ (3588 lb > 2734 lb), higher $\boldsymbol{M_{tip,hover}}$ (0.64 > 0.55) in *Deisgn A* overwhelms it, thus making *Deisgn A* have poor aeroacoustic performance.

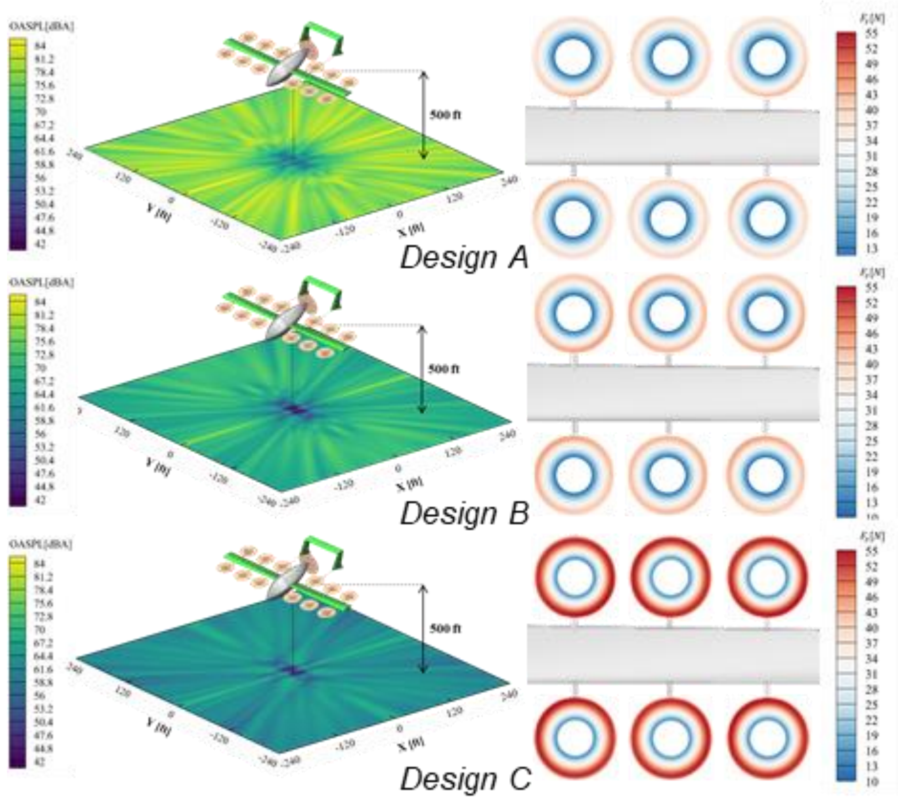

Figure 5-8. Noise contour and lift distribtusion for each design

Through ANOVA and sensitivity analysis, design variables which are dominant in determining $\boldsymbol{GW}$ and $\boldsymbol{L_{Amax}}$ are identified. Among these design variables, $\boldsymbol{\theta_{0,rotor}}$, $\boldsymbol{\theta_{tw,rotor}}$ and $\boldsymbol{R_{rotor}}$ show opposite correlations for $\boldsymbol{GW}$ and $\boldsymbol{L_{Amax}}$. That is, these two design variables show positive correlations with $\boldsymbol{GW}$ and negative correlations with $\boldsymbol{L_{Amax}}$ and this will be validated again through the optimization process in Chapter 6.

Chapter 6. Design optimization

Using this framework, a global design optimization was conducted on a eVTOL aircraft with the lift+cruise configuration. In this study, the design varaibles and the target payload in Table 5-2 that were used in the pramatric design study were used agian in the global design optimization.

Next, the genetic algorithm (GA) was selected as an algorithm for the global design optimization and the optimization was conducted on the surrogate model constructed on Chap. 5.2. GA was adapted since it has advantage of showing good performance for problems with discontinuity and multimodality [54]. Especially, nondominated sorting genetic algorithm II (NSGA-II) was adapted because this algorithm was proved to have good ability of finding Pareto solution set for multiobjective opmization problems by using non-dominated sorting and crowding distance sorting strategies [55]. The opimization process including the GA algorithm was conducted using pymoo library in Python, which is developed for solving optmization problems with multi objective genetic algorithm [56].

Constratins were set to acheive a realistic desgin of the eVTOL aircraft, and $\boldsymbol{GW}$ and $\boldsymbol{L_{Amax}}$ were set as objective functions. Constraints and objective functions are in Table 6-1. Feasibility in the list of constraints means wheter a design can satisfy the target payload or not, and this is determined based on the surrogate model constructed on Chap. 5.2 using GPC.

Table 6-1. Constraints and objectives

Constraints	Rotor-rotor clearance	> 10 % of the rotor radius
	Rotor-wing clearance	> 10 % of the rotor radius
	$M_{tip,rotor}$	< 0.65
	$M_{tip,prop}$	< 0.8
	Feasibility in terms of payload	
Objectives	GW	
	L_{Amax}	

Through the optimization process, 353 Pareto solutions were obtained as shown in Figure 6-1. In addition to Preto points, each point's five most influential design parameters acquired in Chapter 5.2. ($\theta_{0,rotor}$, $\theta_{tw,rotor}$, R_{rotor}, R_{prop} and RPM_{prop}) are shown in Figure 6-1 where each parameter is normalized.

As in Figure 6-1, a clear trade-off relation between GW and L_{Amax} is shown. In addition, as a design change from n = 1 to n = 353, which corresponds to L_{Amax} being reduced and GW being surged, $\theta_{0,rotor}$ increases, R_{rotor} increases, and $\theta_{tw,rotor}$ decreases. This is in accordance with the results from the parametric study. In Chap. 5.2. it was validated that these design variables have significant influences in deciding GW and L_{Amax} ,and they have opposite correlations between these two objectives; these relations are revalidated through the optimization process. On the other hand, $\boldsymbol{R_{prop}}$ and $\boldsymbol{RPM_{prop}}$ remain almost same from n = 1 to n = 353, and again this is a revalidation of the results from the parametric study. Through the paramteric study, it was shown that $\boldsymbol{R_{prop}}$ and $\boldsymbol{RPM_{prop}}$ have strong influences only on $\boldsymbol{GW}$, and as in Figure 6-1, these two design varaibles barely change across Pareto solution sets.

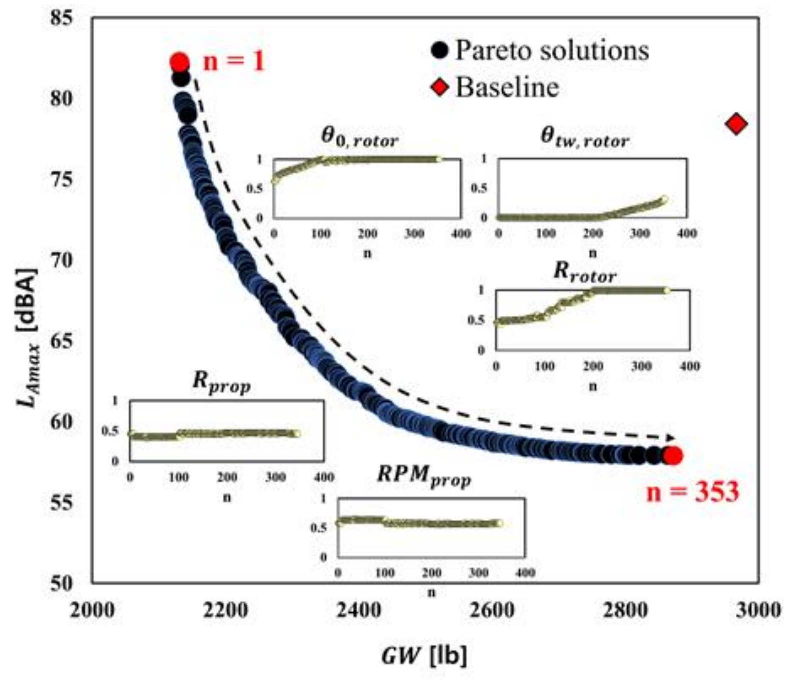

Figure 6-1. Pareto solutions obtained based on surrogate model

Chapter 7. Conclusion

In this study, a design methodology of UAM vehicles for noise mitigation at a conceptual design stage was newly developed. In the new design methodology, a flight analysis module using RISPECT+ & CAMRAD II coupling was used to predict aerodyanmic force distribution accurately, therefore accurate noise prediction is possible. In addition, for fast noise calculation at the conceptual design stage, noise prediction module with compact loading assumption and dual compact loading assumption was used. By using this noise mudule, noise impact of an eVTOL aircraft can be evaluated in a short time. Using the new methodology, parametric study and design optimization were conducted and physical insights of desigining eVTOL aircraft when considering both the gross weight and noise impact were acquired.

First, design variables related with hovering performance have opposite correlations for the hovering tip Mach number and gross weight of eVTOL aircraft. Second, even though tip Mach number and gross weight change in opposite directions, the effect on noise impact by the tip Mach number change overwhelms that by the gross weight change. Finally, because of the two reasons just mentioned, the gross weight and the noise impact have trade-off relation when desigining eVTOL aircraft.

As a future work, validation and improvement of CAMRAD II model using computation fluid dynamics (CFD) simulations is being considered. By conducting validation and improvemnet procedure, it is expected that the methodology becomes more accurate and realistic.

References

[1] Holden, J., and Goel, N., "Fast-forwarding to a future of on-demand urban air transportation," *San Francisco, CA*, 2016.

[2] Rizzi, S. A., Huff, D. L., Boyd, D. D., Bent, P., Henderson, B. S., Pascioni, K. A., Sargent, D. C., Josephson, D. L., Marsan, M.,
He, H. B., et al., "Urban air mobility noise: Current practice, gaps, and recommendations," Tech. rep., 2020.

[3] Silva, C., Johnson, W. R., Solis, E., Patterson, M. D., and Antcliff, K. R., "VTOL urban air mobility concept vehicles for technology development," *2018 Aviation Technology, Integration, and Operations Conference*, 2018, p. 3847.

[4] Li, J., Zheng, Y., Rafaelof, M., Ng, H. K., and Rizzi, S. A., "AIRNOISEUAM: An Urban Air Mobility Noise-Exposure Prediction Tool," *INTER-NOISE and NOISE-CON Congress and Conference Proceedings*, Vol. 263, Institute of Noise Control Engineering, 2021, pp. 474–485.

[5] Clarke, M. A., and Alonso, J., "Evaluating the Performance and Acoustic Footprint of Aircraft for Regional and Urban Air Mobility," *AIAA Aviation 2021 Forum*, 2021, p. 3205.

[6] Sharma, K., "Incorporating acoustic assessment into the design and analysis of rotorcraft," 2016.

[7] Faulkner, H. B., "The cost of noise reduction in helicopters," Tech. rep., Cambridge, Mass.: Massachusetts Institute of Technology, Flight . . . , 1971.

[8] Jaworski, T., "Development of an Acoustic Prediction System for Conceptual Design and Analysis of Rotorcraft," 2021.

[9] Zhou, W., Ning, Z., Li, H., and Hu, H., "An experimental investigation on rotor-to-rotor interactions of small UAV propellers," *35th AIAA applied aerodynamics conference*, 2017, p. 3744.

[10] Shukla, D., and Komerath, N., "Multirotor drone aerodynamic interaction investigation," *Drones*, Vol. 2, No. 4, 2018, p. 43.

[11] Shukla, D., Hiremath, N., and Komerath, N. M., "Low Reynolds number aerodynamics study on coaxial and quad-rotor," *2018 Applied Aerodynamics Conference*, 2018, p. 4118.

[12] Healy, R., Gandhi, F., and Mistry, M., "Computational Investigation of Multirotor Interactional Aerodynamics with Hub Lateral and Longitudinal Canting," *AIAA Journal*, Vol. 60, No. 2, 2022, pp. 872–882.

[13] "Computational Fluid Dynamics (CFD) Solver | Altair AcuSolve," https://www.altair.com.es/Product/AcuSolve/

[14] Ventura Diaz, P., and Yoon, S., "High-fidelity computational aerodynamics of multi-rotor unmanned aerial vehicles," *2018 AIAA Aerospace Sciences Meeting*, 2018, p. 1266.

[15] Alvarez, E. J., Schenk, A., Critchfield, T., and Ning, A., "Rotor-on-rotor aeroacoustic interactions of multirotor in hover," *Journal of the American Helicopter Society*, 2020.

[16] Brown, R. E., and Line, A. J., "Efficient high-resolution wake modeling using the vorticity transport equation," *AIAA journal*, Vol. 43, No. 7, 2005, pp. 1434–1443.

[17] Brown, R. E., "Are eVTOL aircraft inherently more susceptible to the vortex ring state than conventional helicopters?" *48th European Rotorcraft Forum*, 2022.

[18] Alvarez, E. J., and Ning, A., "High-fidelity modeling of multirotor aerodynamic interactions for aircraft design," *AIAA Journal*, Vol. 58, No. 10, 2020, pp. 4385–4400.

[19] Lee, H., and Lee, D.-J., "Rotor interactional effects on aerodynamic and noise characteristics of a small multirotor unmanned aerial vehicle," *Physics of Fluids*, Vol. 32, No. 4, 2020, p. 047107.

[20] QUACKENBUSH, T., and BLISS, D., "Free wake calculation of rotor flow fields for interactional aerodynamics," *AHS, Annual Forum, 44 th, Washington, DC*, 1988.

[21] Pettingill, N. A., and Zawodny, N. S., "Identification and prediction of broadband noise for a small quadcopter," *75th Annual Forum & Technology Display*, 2019.

[22] Guan, S., Lu, Y., Su, T., and Xu, X., "Noise attenuation of quadrotor using phase synchronization method," *Aerospace Science and Technology*, Vol. 118, 2021, p. 107018.

[23] Jeong, J., Ko, J., Cho, H., and Lee, S., "Random process-based stochastic analysis of multirotor hovering noise under rotational speed fluctuations," *Physics of Fluids*, Vol. 33, No. 12, 2021, p. 127107.

[24] Conley, S., and Shirazi, D., “Comparing Simulation Results from CHARM and RotCFD to the Multirotor Test Bed Experimental Data,” *AIAA AVIATION 2021 FORUM*, 2021, p. 2540.
[25] Landgrebe, A. J., “An analytical method for predicting rotor wake geometry,” *Journal of the American Helicopter Society*, Vol. 14, No. 4, 1969, pp. 20–32.
[26] Clark, D. R., and Leiper, A. C., “The free wake analysis,” *Journal of the American Helicopter Society*, Vol. 15, No. 1, 1970, pp. 3–11.
[27] Landgrebe, A. J., “An analytical and experimental investigation of helicopter rotor hover performance and wake geometry characteristics,” Tech. rep., United aircraft research labs east hartford CT, 1971.
[28] Sadler, S. G., “Development and application of a method for predicting rotor free wake positions and resulting rotor blade air loads. Volume 1: Model and results,” Tech. rep., NASA, 1971.
[29] Landgrebe, A. J., “The wake geometry of a hovering helicopter rotor and its influence on rotor performance,” *Journal of the American Helicopter society*, Vol. 17, No. 4, 1972, pp. 3–15.
[30] Scully, M., “Computation of helicopter rotor wake geometry and its influence on rotor harmonic airloads,” Ph.D. thesis, Massachusetts Institute of Technology, 1975.
[31] Bagai, A., and Leishman, J. G., “Rotor Free-Wake Modeling Using a Pseudo-Implicit Technique—Including Comparisons with Experimental Data,” *Journal of the American Helicopter Society*, Vol. 40, No. 3, 1995, pp. 29–41.
[32] Bagai, A., and Leishman, J. G., “Adaptive grid sequencing and interpolation schemes for helicopter rotor wake analyses,” *AIAA journal*, Vol. 36, No. 9, 1998, pp. 1593–1602.
[33] Leishman, J. G., Bhagwat, M. J., and Bagai, A., “Free-vortex filament methods for the analysis of helicopter rotor wakes,” *Journal of aircraft*, Vol. 39, No. 5, 2002, pp. 759–775.
[34] Pascioni, K., and Rizzi, S. A., “Tonal noise prediction of a distributed propulsion unmanned aerial vehicle,” *2018 AIAA/CEAS Aeroacoustics Conference*, 2018, p. 2951.
[35] Johnson, W., and Silva, C., “NASA concept vehicles and the engineering of advanced air mobility aircraft,” *The Aeronautical Journal*, Vol. 126, No. 1295, 2022,

pp. 59–91.
[36]“untitled,”http://johnson
aeronautics.com/documents/CAMRADIIvolumeVII.pdf, (Accessed on 02/02/2023).
[37] Lee, D., Lim, D., and Yee, K., “Generic design methodology for vertical takeoff and landing aircraft with hybrid-electric propulsion,” *Journal of Aircraft*, Vol. 59, No. 2, 2022, pp. 278–292. 13

[38] Lee, D., Lim, D., Yee, K., “Generic Design Methodology for Vertical Takeoff and Landing Aircraft with Hybrid-Electric Propulsion,” Journal of Aircraft, Vol. 59, No. 2, August 2021.

[39] Lee, D., and Yee, K., “Advanced Analysis Method of Electric Propulsion System for UAM Vehicles,” *Proceedings of the 47th European Rotorcraft Forum*, Sept. 7–9, 2021, Virtual.

[40] Lee, S., Ko, B., Ahn, S., Hwang, H., “Initial Sizing of a Tilt Ducted Fan Type eVTOL for Urban Air Mobility,” Journal of Korean Society for Aviation and Aeronautics, Vol. 29, No. 3, 2021, pp. 52-65.

[41] Liu, Q., “Analysis, design and control of permanent magnet synchronous motors for wide-speed operation,” Ph.D. Dissertation, National University of Singapore, 2005.

[42] Lee, D., Kang, S., and Yee, K., “A Comparison Study of Rotorcraft with Hybrid Electric Propulsion System,” Proceedings of the 45th European Rotorcraft Forum, Warsaw, Poland, September 17–20, 2018.

[43] Hassan, W., Wang, B., “Efficiency optimization of PMSM based drive system,” Proceedings of the 7th International Power Electronics and Motion Control Conference, Vol. 2, June 2012, pp. 1027-1033.

[44] Mestha, L., Evans, P., Analysis of on-state losses in PWM inverters. Electric Power Applications,” IEEE Proceedings B, Vol. 136, No.4, 1989, pp.189–195.

[45] Misra, A., “Summary of 2017 NASA Workshop on Assessment of Advanced Battery Technologies for Aerospace Applications,” NASA Glenn Research Center Report, Cleveland, Ohio, January 2018, pp. 1–18.

[46] Farassat, F., Brentner, K., “The Acoustic Analogy and the Prediction of the

Noise of Rotating Blades," Theoretical and Computational Fluid Dynamics, Vol. 10, 1997, pp. 155-170.

[47] Brentner, K., Jones, H., "Noise Prediction for Maneuvering Rotorcraft," AIAA Aeroacoustics Conference, Hampton, Virginia, June 12-14, 2000.

[48] Yang, T., Brentner, K., Walsh, G., "A Dual Compact Model for Rotor Thickness Noise Prediction", American Helicopter Society Journal, Vol. 63, No. 2, April 2018, pp. 12-23.

[49] Brentner, K., Farassat, F., "Modeling Aerodynamically Generated Sound of Helicopter Rotors, " Progress in Aerospace Science, Vol. 39, 2003, pp. 83-120.

[50] Vegh, J., Botero, E., Clarke, M., Trent, J., Alonso, J., "Current Capabilities and Challenges of NDARC and SUAVE for eVTOL Aircraft Design and Analysis," AIAA Propulsion and Energy 2019 Forum, AIAA Paper 2019-4505, Aug. 2019.

[51] McKay, M., Beckman, R., Conover, W., "A Comparison of Three Methods for Selecting Values of Input Variables in the Analysis of Output from a Computer Code," American Statistical Association, Vol. 21, No. 2, May 1979, pp. 239–245

[52] Rasmussen, C., Williams, K., "Gaussian Processes for Machine Learning," the MIT Press, 2006.

[53] Sobol, I., "Global Sensitivity Indices for Nonlinear Mathematical Models and Their Monte Carlo Estimates," Mathematics and Computers in Simulation, Vol. 55, No. 1, February 2001, pp. 271-280.

[54] Sasaki, D., Obayashi, S., "Efficient Search for Trade-Offs by Adaptive Range Multi-Objective Genetic Algorithms," Journal of Aerospace Computing, Information and Communication, Vol. 2, No. 1, January 2005, pp. 44–64.

[55] Deb, K., Pratap, A., Agarwal, S., Meyarivan, T., "A Fast and Elitist Multiobjective Genetic Algorithm : NSGA-II," IEEE Transactions on Evolutionary Computation, Vol. 6, No. 2, April 2002, pp. 182-197.

[56] Blank, J., Deb, K., "pymoo: Multi-Objective Optimization in Python," IEEE Access, Vol. 8, 2020, pp. 89497-89509

국문 초록

이 논문은 개념 설계 단계에서 소음 저감을 위한 UAM 기체의 설계 방법론을 제안하고, 정확한 소음 예측을 위한 로터 해석 모듈과 개념 설계 단계에서의 소음 예측 모듈을 구축한다. 로터 해석 모듈은 로터 블레이드 주변의 공기역학적 힘 분포를 정확하게 예측하기 위해 개발되어 정확한 소음 예측이 가능한데, 이 모듈은 BEMT 또는 BET 방법과 CAMRAD II 를 이용한 로터 해석으로 구성되며, 이 방법들은 공력 분포 데이터를 교환하며, 각 방법에 의한 공력 분포가 수렴될 때까지 계산이 반복된다. 개념 설계 단계를 위한 소음 예측 모듈은 compact 가정과 dual compact 가정을 사용하므로, 하중 및 두께 소음 예측이 단시간에 완료된다. 제안된 설계 방법론은 리프트+크루즈 개념의 eVTOL 항공기의 개념 설계에 적용되고, 설계 최적화 과정을 통해 개념 설계 단계에서 소음 영향을 고려할 필요성이 입증된다.

Advanced Air Mobility, Electric Vertical Takeoff and Landing Aircraft, Noise Prediction, Conceptual Design, Aerodynamic Coupling, Design Optimization

주요어: 차세대 항공교통, 전기동력 수직이착륙 항공기, 소음해석, 항공기 개념설계, 공력 커플링, 설계 최적화

학번: 2021-21121

성명: 김호진